

Microstructure, Tensile Properties and Work Hardening Behavior of GTA-Welded Dual-Phase Steels

H. Ashrafi, M. Shamanian, R. Emadi, and N. Saeidi

(Submitted May 2, 2016; in revised form December 5, 2016; published online February 13, 2017)

In the present study, microstructure, tensile properties and work hardening behavior of a DP700 steel after gas tungsten arc welding were investigated. Formation of bainite in the fusion zone resulted in a hardness increase compared to that for the base metal (BM), whereas tempering of the pre-existing martensite in the subcritical heat-affected zone (HAZ) led to softening. The GTA-welded joint exhibited a continuous yielding behavior and a yield strength close to that for the BM, while its ultimate tensile strength and total elongation were lower than those for the BM owing to the formation of soft zone in the HAZ. A joint efficiency of about 81% was obtained for the GTA-welded joint, and it failed in the softened HAZ. Analysis of work hardening based on the Kocks-Mecking approach showed one stage of hardening behavior corresponding to the stage III for both the DP700 BM and welded sample. It was also revealed that the DP700 BM has larger values of work hardening exponent and magnitude of work hardening compared with the welded sample. Analysis of fractured surfaces showed that the dominant fracture mode for both the DP700 BM and welded joint was ductile.

Keywords dual-phase steel, gas tungsten arc welding, martensite, microstructure, tensile properties, work hardening

1. Introduction

Dual-phase (DP) steels are low-carbon and low-alloy steels consisting of usually 10–30 vol.% of martensite islands distributed in a ductile ferrite matrix (Ref 1, 2). Such a microstructure is created by intercritical annealing or by controlled cooling after hot rolling (Ref 3). These steels are currently used in the automotive industry due to their combination of special mechanical properties such as high tensile strength, low yield strength (YS) to ultimate tensile strength (UTS) ratio, high initial work hardening rate as well as good ductility (Ref 4, 5). The application of DP steels has been one of the major ways to reduce the vehicle weight and fuel consumption, while improving its crashworthiness (Ref 6).

The structural components of automobiles are commonly joined by welding, which plays a significant role in determining the final mechanical properties of material. Hence, it is essential to understand the metallurgical and mechanical phenomena involved in the welding of DP steels (Ref 7). In recent years, effect of the resistance spot welding and laser welding (LW) processes on the microstructure and mechanical properties of DP steels has been extensively studied (Ref 8–12). These studies demonstrated that the subcritical area of the heat-affected zone (HAZ) softens during welding and a mainly martensitic microstructure forms in the weld metal (WM) after

welding, which both can degrade the formability of the welded steel (Ref 13).

Gas tungsten arc welding (GTAW) is a simple and low-cost welding method which is widely used to join different metals and alloys (Ref 14, 15). However, this process has limited applications in automobile manufacturing and is mainly considered as an alternative method to LW in the joining of steel sheet blanks (Ref 16). So far, only a few studies have been devoted to the investigation of microstructure and tensile properties of DP steels after GTAW. Tiziani et al. (Ref 17) investigated the influence of three different welding technologies, GTAW, plasma arc welding (PAW) and electron beam welding, on the properties of DP600 steel. The GTA-welded sample exhibited the highest amount of softening in the HAZ and the lowest value of UTS. However, differences between the properties of GTAW and PAW samples were not too great. Lee et al. (Ref 16) investigated the microstructural characteristics, tensile properties and low-cycle fatigue behavior of a DP780 steel following joining by three methods: LW, tungsten inert gas (TIG) welding, and metal active gas (MAG) welding. Their results showed that TIG welding can lead to tensile and fatigue properties comparable to those for LW. The mechanical properties of TIG-welded sample were greater than those of MAG welded sample.

Despite its simplicity and low cost, GTAW has allocated little attention in the joining of DP steels and literature about the GTAW of DP steels is limited. Therefore, the present study aimed to investigate the microstructure, tensile properties and work hardening behavior of a cold-rolled DP700 steel after GTAW.

2. Experimental Procedure

2.1 Base Material

The material used in this study was a 2-mm-thick sheet of DP700 steel (0.18% C, 1.25% Mn, 0.2% Si).

H. Ashrafi, M. Shamanian, R. Emadi, and N. Saeidi, Department of Materials Engineering, Isfahan University of Technology, Isfahan 84156-83111, Iran. Contact e-mail: h.ashrafi@ma.iut.ac.ir.

2.2 Welding Procedure

The material was cut into plates with the dimensions of 150 mm × 40 mm × 2 mm for performing welding trials. Square butt joint design without edge preparation was used so that welding could be accomplished in one pass ensuring full penetration. Before welding the edges were cleaned mechanically and degreased by acetone in order to avoid any source of contamination like scale, rust, oil, etc. which could produce weld defect. The welding was carried out using autogenous GTAW (Fronius Magic Wave 2000) with Direct-Current Electrode Negative (DCEN) mode. Figure 1 shows a schematic representation of the GTAW process. The welding current and voltage were 80 A and 8 V, respectively, and the welding was performed with a constant speed of 1.8 mm/s. These parameters were chosen so that a sound weld with minimum heat input (HI) is achieved. The HI per unit length was calculated using the following relation (Ref 18):

$$HI = \frac{I \times V}{S} \times \eta \quad (\text{Eq 1})$$

where I is the mean current (A), V is the mean voltage (V), S is the welding speed and η is the efficiency of welding process (0.6). Using the above formula, the HI was evaluated to be 0.21 KJ/mm.

Other details related to the process and procedure used in the present study include: diameter of non-consumable tungsten electrode = 2.4 mm, nozzle size = 8 mm, shielding and backing gas type = Argon of 99.9% purity, shielding and backing gas flow rate = 10 L/min. Welding was done from only one side of the joint in one pass along the rolling direction. During and after welding, the joint was visually inspected to ensure that it was free from visible defects.

2.3 Specimen Sampling

The specimens for tensile testing, microhardness and metallography studies were taken from the welded sheets as schematically illustrated in Fig. 2.

2.4 Metallography

In order to study the microstructural changes that takes place during welding, specimens were cut from the weld cross

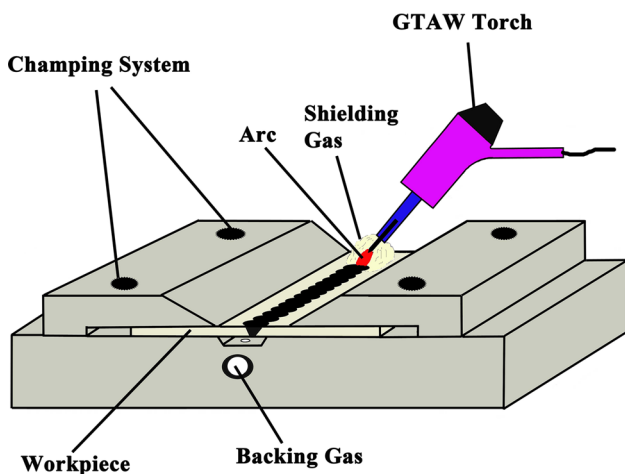


Fig. 1 Schematic representation of GTAW process used in this study

section (Fig. 2). The sectioned specimens were mounted, mechanically grounded to 4000 grit finish, polished with 0.3 μm alumina suspension and etched with 2% Nital solution. The microstructures of etched samples were studied using a Philips XL30 scanning electron microscopy (SEM). The volume fraction of martensite in the BM was measured by point counting method based on the ASTM E562-83 standard (Ref 19), using the image J software.

2.5 Mechanical Properties Characterization

Microhardness measurements were conducted on the cross section of welded sample (Fig. 2) at a load of 100 g with a dwell time of 10 s using a Vickers microhardness tester. The indentations were carried out along the centerline of the sectioned specimen. All the indentations were adequately spaced to avoid any potential effect of strain field caused by adjacent indentations.

For determination of the tensile properties, uniaxial tensile tests were conducted on the BM and welded joint at the cross head speed of 1 mm/min using a Hounsfield H50KS machine. Tensile specimens (Fig. 3) were machined out from the BM and welded sample through electro discharge machining. The finished surfaces of machined specimens were polished to remove any effect of the machining process. For each condition (including BM), three specimens were tested. Fractured surfaces of the tensile tested specimens were examined by SEM to assess the nature of the fracture mode.

3. Results and Discussion

3.1 Calculation of Thermal Cycle During Welding

The thermal cycle experienced by each point during the welding process can strongly affect phase transformations during welding and thus the properties of the welded material. In the present study, the peak temperature and cooling rate across the HAZ were estimated using the heat conduction equations.

Adams equation for calculating the peak temperature (T_p) at the workpiece surface at a distance x away from the fusion line is expressed as (Ref 20):

$$\frac{1}{T_p - T_0} = \frac{4.13gx\rho CS}{Q} + \frac{1}{T_m - T_0} \quad (\text{Eq 2})$$

where T_0 is the workpiece temperature before welding (about 25 °C), g is the sheet thickness (2 mm), x is the distance from the fusion line, ρ is the specific mass (7.87 g/cm³), C is the specific heat ($C = 0.5$ J/gK), S is the welding speed (1.8 mm/s), Q is the welding heat input ($Q = \eta VI$), and T_m is the melting temperature (1500 °C). The cooling cycle in the HAZ was also calculated using the following equation (Ref 21):

$$T - T_0 = \frac{Q}{g\rho CS} \frac{1}{(4\pi\alpha t)^{0.5}} e^{-\frac{x^2}{4\alpha t}} \quad (\text{Eq 3})$$

where α is the thermal diffusivity ($\alpha = k/\rho C$ where k is the thermal conductivity) and t is the time. Bayraktar et al. (Ref 22) showed that Eq 2 and 3 can accurately predict the peak temperature and cooling curve of different locations of HAZ during the GTAW of interstitial free (IF) steel. The calculated

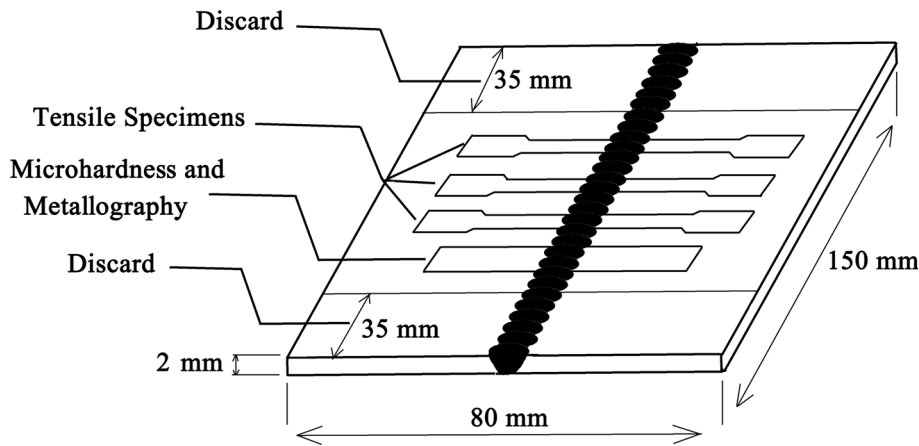


Fig. 2 Schematic illustration of the specimen sampling from the weldment

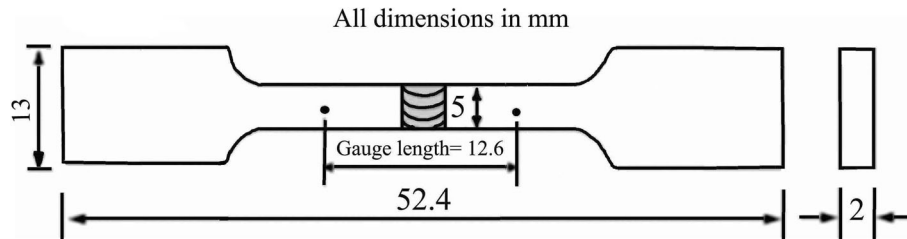


Fig. 3 Dimensions of the tensile test specimens used in the present work

peak temperatures and cooling curves in the HAZ as a function of distance from the fusion line for the current welding process are presented in Fig. 4(a) and (b). As can be seen in Fig. 4(a), the peak temperature in the HAZ gradually decreases with distance from the fusion line. It is also observed in Fig. 4(b) that the cooling rate in the HAZ is in the range of about 25 °C/s (from 800 to 500 °C). It should be noted that the above calculations only give an estimate of the peak temperatures and cooling rate, since the analytical equations are derived using some simplifying assumptions. Ideally, the welding thermal cycles should be experimentally measured at different points of HAZ.

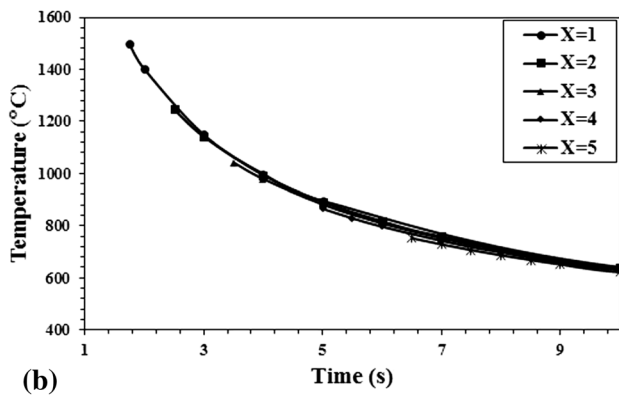
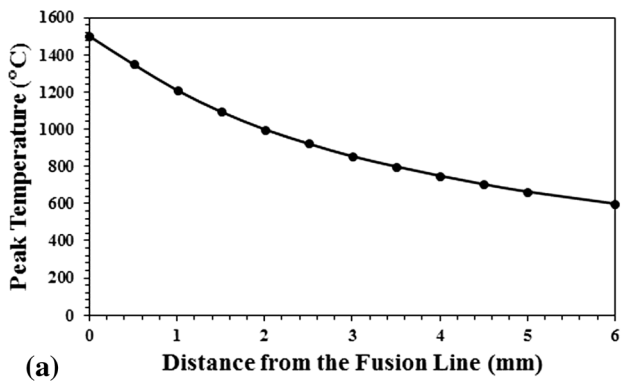
3.2 Microstructural Evolutions

According to the Fe-C phase diagram, the cross section of welded sample can be divided into five different areas: fusion zone (FZ), uppercritical HAZ, intercritical HAZ, subcritical HAZ and unaffected BM. Figure 4(c) shows the peak temperature experienced by each region during the welding. FZ (A-A) is the region in which the peak temperature during the welding is above the melting temperature of steel. In the uppercritical HAZ (A-B), the peak temperature reaches to a temperature above the critical temperature of A_3 . This area can be divided into two sub areas: coarse-grained HAZ (CGHAZ) in which the peak temperature reaches well above the A_3 temperature and is located close to the FZ, and fine-grained HAZ (FGHAZ) which is subjected to a peak temperature just above the A_3 temperature and is located far from the FZ. The peak temperature of the intercritical HAZ (B-C) is in the intercritical temperature region (between A_3 and A_1). In the subcritical HAZ (C-D), the peak temperature is below the critical temperature of A_1 . The BM is not experienced any thermal cycle during the welding.

Different thermal histories in different areas results in various microstructures after welding. The microstructures of different regions after GTAW are discussed in the following.

The SEM micrographs of the microstructures of different regions of the cross section of welded sample are shown in Fig. 5. The microstructure of DP700 BM (Fig. 5a) consists of ~28 vol.% of martensite islands in ferrite matrix. The microstructure in the subcritical HAZ (Fig. 5b) is similar to that for the BM, comprising of ferrite and martensite. However, higher magnification image of martensite in this region indicates that the martensite is partially tempered. In the intercritical HAZ (Fig. 5c), refined ferrite grains, fine pearlite, tempered martensite and unaffected ferrite grains of BM are observed. A bimodal distribution of large and small ferrite grains exists in this region. The FGHAZ consists of small ferrite grains and pearlite colonies (Fig. 5d). The size of ferrite grains in this zone is significantly reduced compared to the BM. The microstructure of CGHAZ (Fig. 5e) is predominantly bainitic with a small amount of ferrite and pearlite. In the FZ (Fig. 5f), a bainitic microstructure with a small amount of grain boundary ferrite is observed.

Figure 6 presents a schematic illustration of microstructural evolutions take place in different zones during the GTAW of DP700 steel. The peak temperature and the cooling rate are the most important parameters governing the microstructural evolutions within each zone (Ref 23). In the subcritical HAZ, the peak temperature during the welding is just below the critical temperature of A_1 . This leads to the tempering of pre-existing martensite. The extent of tempering increases with an increase in the distance from the BM due to the increase in the peak temperature attained by the material (Fig. 4b). The ferrite grains are essentially unaffected. The intercritical HAZ region is subjected to a peak temperature between the critical



- AA: Fusion Zone ($T > T_L$)
- AB: Upper Critical HAZ ($T > A_1$)
- BC: Intercritical HAZ ($A_3 < T < A_1$)
- CD: Subcritical HAZ ($T < A_3$)

Fig. 4 (a) Peak temperature in the HAZ as a function of distance from the fusion line, and (b) cooling curve of different points of HAZ as a function of time and distance from the fusion line. (c) Schematic illustration of various temperature ranges in the cross section of DP700 welded joint

temperatures of A_1 and A_3 . As illustrated in Fig. 6, the martensite islands transform to austenite and expand into the ferrite grains upon heating to above A_1 temperature. These austenite grains decompose into fine grains of ferrite and pearlite during cooling. The volume fraction of pearlite and ferrite increases by moving from the A_1 line (subcritical and intercritical HAZ boundary) toward the A_3 line (boundary between intercritical and uppercritical HAZ). The FGHAZ is subjected to a peak temperature just above the critical temperature of A_3 , allowing fine austenite grains to nucleate. Such austenite grains decompose into fine ferrite and pearlite during the subsequent cooling. The CGHAZ experienced a peak temperature well above the critical temperature of A_3 , allowing austenite grains to grow. The high cooling rate (about 25 °C/s) and large grain size encourage the formation of a mostly bainitic structure. A small number of grain boundary

ferrite is also observed at grain corners of prior austenite. Bainite forms by decomposition of austenite at a temperature which is above M_s , but below that at which pearlite forms (Ref 24). Therefore, bainite can form at cooling rates lower than that is needed for the formation of martensite, but higher than that leads to the formation of pearlite. In the FZ, the peak temperature during the welding exceeds the melting temperature of steel and therefore the BM completely melts. During the cooling cycle, large austenite grains form which completely transform to bainite.

Studies have shown that the microstructure of as-welded DP steels depends on the welding method. Ahiale et al. (Ref 25) observed a microstructure consisted of randomly oriented allotriomorphic ferrite, Widmanstatten ferrite, acicular ferrite and martensite for the FZs of GMA-welded and PA-welded DP590 steel (0.069% C, 1.35% Mn, 0.066% Si) sheets. Tiziani et al. (Ref 16) detected a mixture of acicular ferrite, allotriomorphic ferrite and bainite in the FZ of a 2-mm-thick DP600 steel (0.051% C, 1.025% Mn, 0.287% Si) sheet after joining by GTAW, PAW and electron beam welding methods. Ramazani et al. (26) observed a fully bainitic and a bainitic-ferritic microstructure in the FZ and uppercritical HAZ of a GMA-welded DP600 steel (0.06% C, 0.88% Mn, 0.08% Si), respectively. Jia et al. (Ref 12) obtained a fully martensitic microstructure in the FZ and uppercritical HAZ and a microstructure consisted of ferrite and martensite in the intercritical HAZ of a fiber-laser-welded DP980 (0.15%C, 1.5% Mn, 0.31%Si) steel. In fact, the cooling rate during the LW of DP steels is so high that martensite can form in the FZ and uppercritical HAZ. However, for welding methods with lower power density, the cooling rate is not sufficient to form a martensitic structure. Therefore, the microstructure of FZ and HAZ mainly consists of softer constituents such as bainite and ferrite.

3.3 Microhardness Profile

Figure 7 shows the microhardness profile of the cross section of DP700 steel joint. Each zone is marked in the microhardness profile. The average hardness value of the DP700 BM was measured to be 222 HV. As can be seen, the FZ has higher hardness value (maximum hardness of 290 HV) than the DP700 BM, which is attributed to the formation of a bainitic microstructure. The hardness decreases with the increasing distance from the fusion line and shows the minimum value of 171 HV in the subcritical HAZ. This decrease in hardness with increasing distance from the FZ is caused by the increase in the fraction of ferrite-pearlite constituents in the microstructure. Tempering of the pre-existing martensite in the subcritical HAZ leads to the formation of an area which has a lower hardness than BM. The hardness reduction increases with increasing distance from the BM due to the increase in the peak temperature attained by the material (Fig. 4). The area in which the local hardness drops below the BM hardness is called the softened zone. HAZ softening is unavoidable in DP steels in the subcritical HAZ (Ref 27). The presence of softened zone was previously observed in the LW (Ref 7), resistance spot welding (Ref 28), PAW and GMAW (Ref 25) of DP steels.

3.4 Tensile Properties

Figure 8 shows the representative engineering and true stress-strain curves of the DP700 BM and welded joint. The

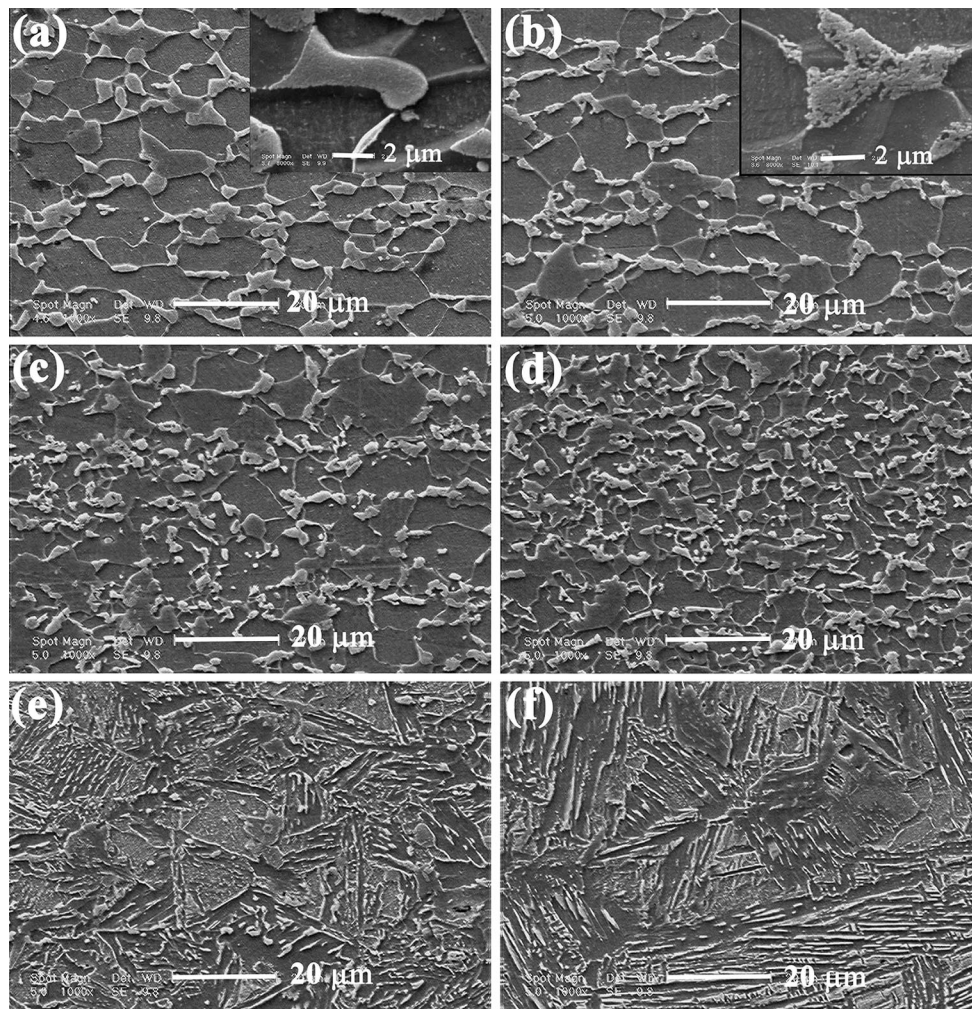


Fig. 5 SEM micrographs of the microstructure of different zones in the cross section of GTA-welded joint, (a) BM, (b) subcritical HAZ, (c) intercritical HAZ, (d) FGHAZ, (e) CGHAZ, and (f) FZ

tensile test results are summarized in Table 1. The DP700 BM shows continuous yielding and low yield ratio, which are the typical characteristics of DP steels (Ref 29). According to Fig. 8 and Table 1, the mechanical properties change significantly after welding. The DP700 joint also exhibits a continuous yielding behavior and a YS close to that for the BM. However, the UTS and total elongation (TE) are considerably reduced compared to those for the BM. As can be seen in Fig. 9, the DP700 joint failed in the subcritical HAZ where the softening was occurred. This suggests that during the tensile testing, strain accumulates in one of the soft zones. Width reduction of tensile tested joint along the gauge was measured to evaluate the local plastic deformation, as shown in Fig. 10. As can be seen, most of the plastic deformation was tolerated by the soft zone, which agrees with the failure site. Therefore, the lower elongation and tensile strength of DP700 joint can be attributed to the localization of strain during deformation. The joint efficiency (the ratio of the UTS of welded sample to the UTS of BM) of current study is 80.84%, which is close to that reported by Tiziani et al. (Ref 16) for the GTAW of DP600 steel (about 84%). However, the percent elongation (the TE of welded sample to the TE of BM) of 56% obtained in the present study is higher than that observed by Tiziani et al. (~43%). For the TIG welding of DP780 steel, joint efficiency and percent

elongation of 97 and 79% were reported, respectively (Ref 17). These better tensile properties compared to the present study is owing to the lower extent of HAZ softening (~20 HV) in TIG-welded DP780 steel compared to that in the current study (~50 HV). The joint efficiency and percent elongation obtained in the present study are also very close to those observed for the GMAW of DP600 steel (~84 and ~54%, respectively). The joint efficiency of current study is lower than the joint efficiency of ~96% reported for LW of DP980 steel (Ref 30). This can be attributed to the formation of a narrower soft zone in the LW compared to the GTAW. However, the percent elongation of ~56% was obtained in the present study which is well above the percent elongation of ~32% obtained for the LW of DP980 steel. This is probably due to the formation of a fully martensitic microstructure in the upper critical HAZ and FZ of laser-welded joint.

3.5 Work Hardening Behavior

The work hardening behavior of BM and welded joint were analyzed based on the Kocks-Mecking approach (Ref 31). Figure 11 shows the variations of instantaneous work hardening rate ($\theta = d\sigma/d\epsilon$) as a function of true stress. In the Kocks-Mecking approach, the evolution of dislocation structure with

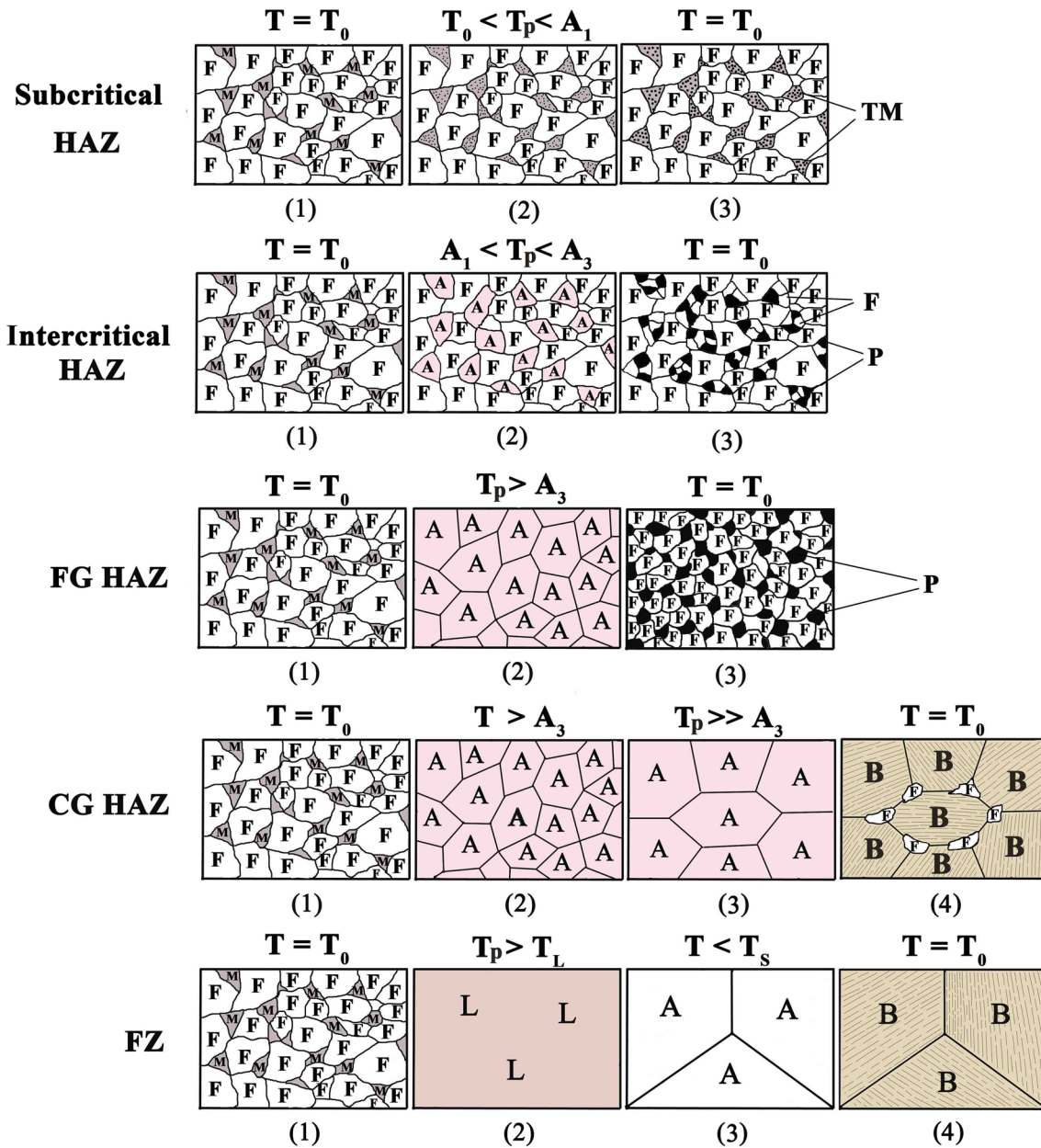


Fig. 6 Schematic illustration of microstructural evolutions in different zones during the GTAW of DP700 steel

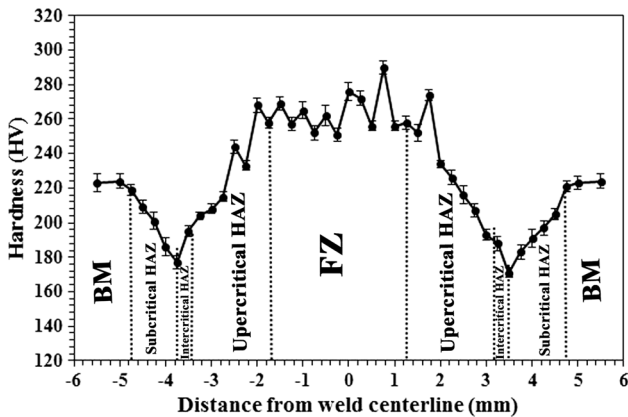


Fig. 7 Microhardness profile of the DP700 steel joint

strain is assumed to be responsible for plastic deformation. The work hardening is controlled by the competition between storage and annihilation of dislocations, and evolution of total dislocation density is assumed to be the governing parameter defining the course of deformation (Ref 32). Both the BM and welded sample show gradual decrease of work hardening rate with stress or stage III hardening (Ref 31). Moreover, a similar value of work hardening rate at the onset of plastic deformation is observed for both the DP700 BM and welded joint. However, as deformation continues, the work hardening rate of welded sample decreases at a higher rate and becomes smaller than that for the DP700 BM. It has been demonstrated that the plastic deformation of DP steels occurs in three stages (Ref 33):

- The first stage at the start of plastic deformation shows rapid work hardening rate because of elimination of residual stresses and rapid buildup of back stress due to the plastic

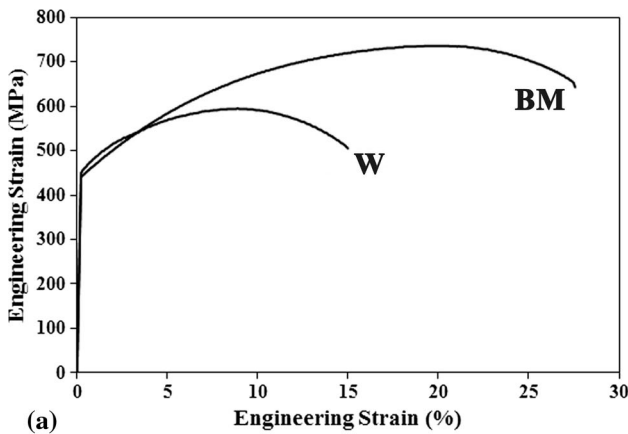
incompatibility of ferrite and martensite.

- As deformation continues, the work hardening rate of ferrite is reduced because the plastic deformation of ferrite is constrained by hard martensite particles. Stress transfer from ferrite to martensite occurs in this stage and the work hardening rate decreases.
- At the final stage of deformation, dislocation cell structure is formed and further deformation in the ferrite is governed by dynamic recovery and cross-slip and by yielding of martensite phase.

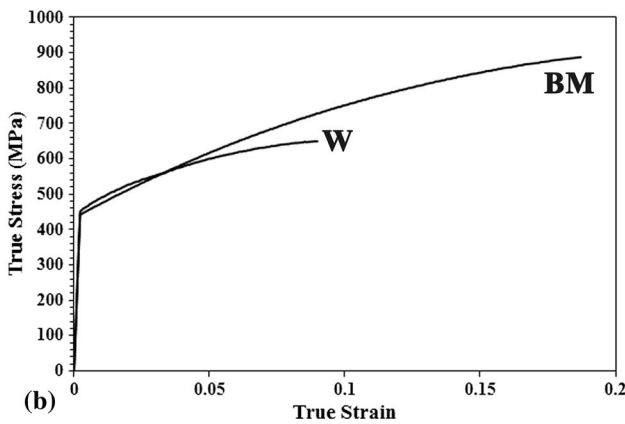
In the previous section, the minimum hardness in the cross section of welded sample was observed in the subcritical HAZ, which consists of ferrite and tempered martensite. Because of its minimum hardness, the yielding first occurs in the subcritical HAZ and the plastic deformation would be accumulated in this zone. Since at the start of plastic flow only the ferrite deforms plastically, both the DP700 BM and welded joint exhibit a similar work hardening rate. However, with further deformation, the martensite phase also yields and plastically deforms. It



Fig. 9 Fracture locations for the tensile tested specimens (1: BM, 2: welded sample)



(a)



(b)

Fig. 8 (a) Engineering and (b) true stress-strain curves of DP700 BM and GTA-welded sample (W)

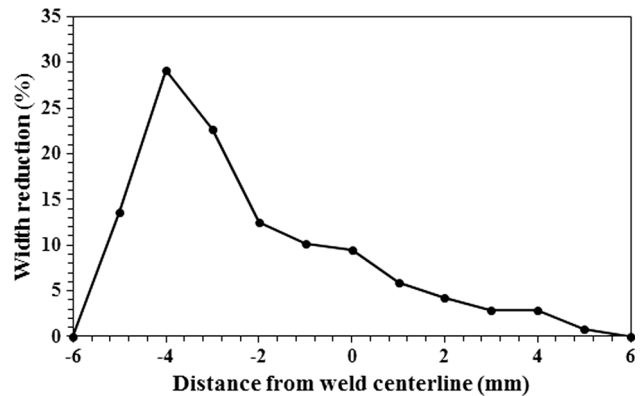


Fig. 10 Width reduction of different areas after tensile testing of DP700 welded joint

is well known that the plasticity of martensite increases after

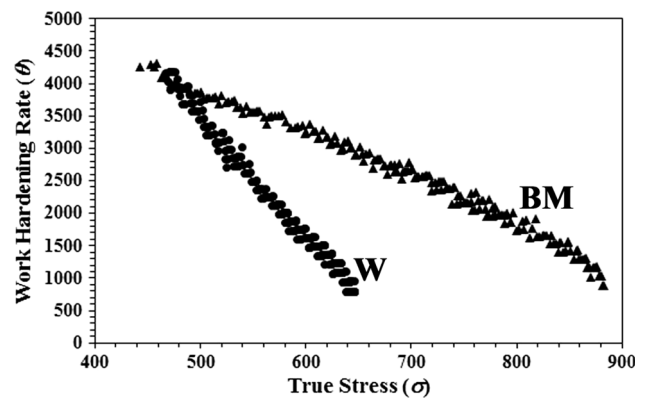


Fig. 11 Variations of work hardening rate (θ) vs. true stress for the DP700 BM and GTA-welded joint

Table 1 Summary of the tensile properties of DP700 BM and GTA-welded sample

Sample	YS, MPa	UTS, MPa	TE, %	UTS \times TE, MPa%	Joint efficiency, %
DP700-BM	441 \pm 7	736 \pm 5	27.56 \pm 0.31	20,284	...
DP700-Weld	450 \pm 12	594 \pm 10	15.49 \pm 0.7	9201	80.84

Table 2 The values of work hardening magnitude and work hardening exponents of Hollomon (n) and Ludwik (m) equations for the DP700 BM and GTA-welded joint

Sample	Work hardening magnitude, MPa	n	m
DP700-BM	295	0.23	0.56
DP700-Weld	144	0.13	0.44

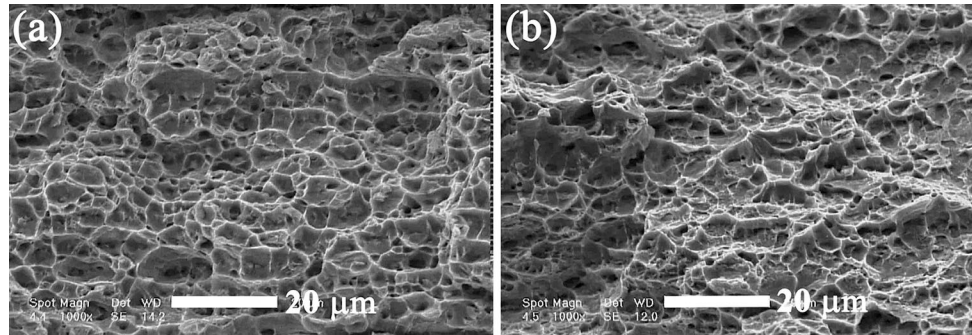


Fig. 12 SEM micrograph of the fractured surface of tensile tested specimens, (a) DP700 BM, (b) welded sample

tempering (Ref 34). The higher plasticity of tempered martensite in the subcritical HAZ of DP700 joint leads to a lower work hardening rate. Farabi et al. (Ref 12) also observed the stage III work hardening behavior for the DP600 steel and DP980 laser-welded joints. In contrast, Jia et al. (Ref 35) reported two stages of work hardening corresponding to stage III and stage IV for the tensile behavior of fiber-laser-welded DP980 steel joint. It should be mentioned that since the welded joint is an inhomogeneous material, the Kocks-Mecking analysis of work hardening may not be accurate for the welded sample and some finite element analysis are needed to accurately describe the deformation behavior of welded joint.

After yielding, the flow curve in the uniform deformation stage can be expressed by one of the following relations:

(1) Hollomon equation (Ref 36):

$$\sigma = k\varepsilon^n \quad (\text{Eq 4})$$

Ludwik equation (Ref 37):

$$\sigma = \sigma_0 + k\varepsilon^m \quad (\text{Eq 5})$$

where σ and ε are true stress and true strain, k is a constant and n and m are work hardening exponents. Work hardening exponent is a good indicator for work hardenability of the material. The higher the value of work hardening exponent, the higher is the rate at which the material work hardens. A material with a high value of work hardening exponent is preferred for processes involving plastic deformation. The larger the work hardening exponent value, the more the material can deform before instability, and the material can be stretched further before necking starts (Ref 38).

Table 2 presents the values of the work hardening exponents of Hollomon and Ludwik equations and magnitude of work hardening for the DP700 BM and welded joint. The values of work hardening exponents were evaluated by fitting the true stress-strain curves to the above equations. As can be seen, the DP700 BM has larger values of work hardening exponents and magnitude of work hardening compared with the welded

sample. This indicates that the formability of DP700 steel degrades after GTAW.

3.6 Fractography Analysis

SEM fractographs of the tensile tested specimens are illustrated in Fig. 12. Dimples are observed in the fracture surface of both DP700 BM and welded joint, indicating that the major fracture mechanism is ductile. It has been demonstrated that the ductile fracture in DP steels occurs in three stages: void nucleation, void growth and void coalescence resulting in a dimpled fracture surface (Ref 39). Microvoid formation occurs by different mechanisms: decohesion at the ferrite-martensite interface, martensite cracking and martensite necking (Ref 40). The dimple size distribution of the fracture surface of welded sample is more non-uniform than that for the DP700 BM, which can be attributed to the localization of plastic deformation in the subcritical HAZ of DP700 joint and lower elongation of this sample.

4. Conclusions

In the present study, effect of GTAW on the microstructure, tensile properties and work hardening behavior of a DP700 steel was investigated. The main conclusions can be summarized as follows:

1. The microstructure of DP700 steel after GTAW consisted of bainite in the fusion zone and coarse-grained HAZ, fine ferrite-pearlite in the fine-grained HAZ, undissolved ferrite and fine ferrite-pearlite in the intercritical HAZ and ferrite and tempered martensite in the subcritical HAZ. Formation of bainite in fusion zone led to an increase in the hardness, whereas tempering of pre-existing martensite in the subcritical HAZ and formation of ferrite-pearlite in the intercritical HAZ caused the hardness

to locally decrease to values below the hardness value of the DP700 BM.

2. The DP700 steel joint exhibited a continuous yielding behavior and a YS close to that for the BM with a lower UTS, UE and TE. The joint efficiency of GTA-welded material was ~81%, and this sample failed in the subcritical HAZ which had the minimum hardness value.
3. Analysis of work hardening based on the Kocks-Mecking approach showed one stage of hardening behavior corresponding to the stage III for both the DP700 BM and GTA-welded sample. It was also revealed that the DP700 BM has larger values of work hardening exponents and magnitude of work hardening compared with the GTA-welded joint.
4. Both the DP700 BM and welded joint exhibited a ductile fracture mode. The dimple size distribution on the fracture surface of welded sample was more non-uniform than that for the DP700 BM.

Based on the results obtained in this study, it is concluded that GTAW can be considered as a suitable method for welding of DP steels. However, further studies are still needed to investigate other properties of GTA-welded DP steels such as formability and fatigue behavior.

References

1. K. Park, M. Nishiyama, N. Nakada, T. Tsuchiyama, and S. Takaki, Effect of the Martensite Distribution on the Strain Hardening and Ductile Fracture Behaviors in Dual-Phase Steel, *Mater. Sci. Eng. A*, 2014, **604**, p 135–141
2. A.G. Kalashami, A. Kermanpur, A. Najafizadeh, and Y. Mazaheri, Effect of Nb on Microstructures and Mechanical Properties of an Ultrafine-Grained Dual Phase Steel, *J. Mater. Eng. Perform.*, 2015, **24**, p 3008–3017
3. Y. Cao, B. Karlsson, and J. Ahlström, Temperature and Strain Rate Effects on the Mechanical Behavior of Dual Phase Steel, *Mater. Sci. Eng. A*, 2015, **636**, p 124–132
4. H. Ghassemi-Armaki, R. Maaß, S.P. Bhat, S. Sriram, J.R. Greer, and K.S. Kumar, Deformation Response of Ferrite and Martensite in a Dual-Phase Steel, *Acta Mater.*, 2014, **62**, p 197–211
5. W. Wang and X. Wei, The Effect of Martensite Volume and Distribution on Shear Fracture Propagation of 600–1000 MPa Dual Phase Sheet Steels in the Process of Deep Drawing, *Int. J. Mech. Sci.*, 2013, **67**, p 100–107
6. S. Winkler, A. Thompson, C. Salisbury, M. Worswick, I.V. Riemsdijk, and R. Mayer, Strain Rate and Temperature Effects on the Formability and Damage of Advanced High-Strength Steels, *Metall. Mater. Trans. A*, 2008, **39**, p 1350–1358
7. Y. Liu, D. Dong, L. Wang, X. Chu, P. Wang, and M. Jin, Strain Rate Dependent Deformation and Failure Behavior of Laser Welded DP780 Steel Joint Under Dynamic Tensile Loading, *Mater. Sci. Eng. A*, 2015, **627**, p 296–305
8. V.H.B. Hernandez, S.K. Panda, M.L. Kuntz, and Y. Zhou, Nanoindentation and Microstructure Analysis of Resistance Spot Welded Dual Phase Steel, *Mater. Lett.*, 2010, **64**, p 207–210
9. B. Wang, L. Hua, X. Wang, Y. Song, and Y. Liu, Effects of Electrode Tip Morphology on Resistance Spot Welding Quality of DP590 Dual-Phase Steel, *Int. J. Adv. Manuf. Technol.*, 2016, **83**, p 1917–1926
10. C. Ma, D.L. Chen, S.D. Bhole, G. Boudreau, A. Lee, and E. Biro, Microstructure and Fracture Characteristics of Spot-Welded DP600 Steel, *Mater. Sci. Eng. A*, 2008, **485**, p 334–346
11. D. Parkes, W. Xu, D. Westerbaan, S.S. Nayak, Y. Zhou, F. Goodwin, S. Bhole, and D.L. Chen, Microstructure and Fatigue Properties of Fiber Laser Welded Dissimilar Joints Between High Strength Low Alloy and Dual-Phase Steels, *Mater. Des.*, 2013, **51**, p 665–675
12. N. Farabi, D.L. Chen, and Y. Zhou, Tensile Properties and Work Hardening Behavior of Laser-Welded Dual-Phase Steel Joints, *J. Mater. Eng. Perform.*, 2012, **21**, p 222–230
13. S.K. Panda, M.L. Kuntz, and Y. Zhou, Finite Element Analysis of Effects of Soft Zones on Formability of Laser Welded Advanced High Strength Steels, *Sci. Technol. Weld. Join.*, 2009, **14**, p 52–61
14. A. Ravikiran, S.K. Velaga, G. Rajput, and S. Venugopal, Influence of Welding Speed and Power On Residual Stress During Gas Tungsten Arc Welding (GTAW) of Thin Sections with Constant Heat Input: A Study Using Numerical Simulation and Experimental Validation, *J. Manuf. Process.*, 2014, **16**, p 200–211
15. Z. Yang, B. Qi, B. Cong, F. Liu, and M. Yang, Microstructure, Tensile Properties of Ti-6Al-4V by Ultra High Pulse Frequency GTAW with Low Duty Cycle, *J. Mater. Process. Technol.*, 2015, **216**, p 37–47
16. J.H. Lee, S.H. Park, H.S. Kwon, G.S. Kim, and C.S. Lee, Laser, Tungsten Inert Gas, and Metal Active Gas Welding of DP780 Steel: Comparison of Hardness, Tensile Properties and Fatigue Resistance, *Mater. Des.*, 2014, **64**, p 559–565
17. A. Tiziani, P. Ferro, R. Cervo, and M. Durante, Effects of Different Welding Technologies on Metallurgical and Mechanical Properties of DP600 Steel Welded Joints, *La Metall. Ital.*, 2011, **1**, p 27–34
18. P.K. Giridharan and N. Murugan, Optimization of Pulsed GTA Welding Process Parameters for the Welding of AISI, 304L Stainless Steel Sheets, *Int. J. Adv. Manuf. Technol.*, 2009, **40**, p 478–489
19. ASTM E562, *Determining Volume Fraction by Systematic Manual Point Count, Annual Book of ASTM Standards*, American Society for Testing and Materials, 2004
20. S. Kou, *Welding Metallurgy*, Wiley, Hoboken, 2003
21. M. Xia, E. Biro, Z. Tian, and Y.N. Zhou, Effects of Heat Input and Martensite on HAZ Softening in Laser Welding of Dual Phase Steels, *ISIJ Int.*, 2008, **48**, p 809–814
22. E. Bayraktar, D. Kaplan, L. Devillers, and J.P. Chevalier, Grain Growth Mechanism During the Welding of Interstitial Free (IF) Steels, *J. Mater. Process. Technol.*, 2007, **189**, p 114–125
23. W. Guo, D. Crowther, J.A. Francis, A. Thompson, Z. Liuc, and L. Li, Microstructure and Mechanical Properties of Laser Welded S960 High Strength Steel, *Mater. Des.*, 2015, **85**, p 534–548
24. Z.G. Yang and H.S. Fang, An Overview on Bainite Formation in Steels, *Curr. Opin. Solid State Mater. Sci.*, 2005, **9**, p 277–286
25. G.K. Ahiale, Y.J. Oh, W.D. Choi, K.B. Lee, J.G. Jung, and S.W. Nam, Microstructure and Fatigue Resistance of High Strength Dual Phase Steel Welded with Gas Metal Arc Welding and Plasma Arc Welding Processes, *Met. Mater. Int.*, 2013, **19**, p 933–939
26. A. Ramazani, K. Mukherjee, U. Prah, and W. Bleck, Transformation-Induced, Geometrically Necessary, Dislocation-Based Flow Curve Modeling of Dual-Phase Steels: Effect of Grain Size, *Metall. Mater. Trans. A*, 2012, **43**, p 3850–3869
27. D. Dong, Y. Liu, Y. Yang, J. Li, M. Ma, and T. Jiang, Microstructure and Dynamic Tensile Behavior of DP600 Dual Phase Steel Joint by Laser Welding, *Mater. Sci. Eng. A*, 2014, **594**, p 17–25
28. V.H.B. Hernandez, S.K. Panda, Y. Okita, and N.Y. Zhou, A Study on Heat Affected Zone Softening in Resistance Spot Welded Dual Phase Steel by Nanoindentation, *J. Mater. Sci.*, 2010, **45**, p 1638–1647
29. Z. Sami, S. Tahar, and H. Mohamed, Microstructure and Charpy Impact Properties of Ferrite-Martensite Dual Phase API, X70 Linepipe Steel, *Mater. Sci. Eng. A*, 2014, **598**, p 338–342
30. W. Xu, D. Westerbaan, S.S. Nayak, D.L. Chen, F. Goodwin, and Y. Zhou, Tensile and Fatigue Properties of Fiber Laser Welded High Strength Low Alloy and DP980 Dual-Phase Steel Joints, *Mater. Des.*, 2013, **43**, p 373–383
31. U.F. Kocks and H. Mecking, Physics and Phenomenology of Strain Hardening: The FCC Case, *Prog. Mater. Sci.*, 2003, **48**, p 171–273
32. G. Sainath, B.K. Choudhary, J. Christopher, E.I. Samuel, and M.D. Mathew, Applicability of Voce Equation for Tensile Flow and Work Hardening Behaviour of P92 Ferritic Steel, *Int. J. Press. Ves. Pip.*, 2015, **132–133**, p 1–9
33. E. Ahmad, T. Manzoor, M.M.A. Ziai, and N. Hussain, Effect of Martensite Morphology on Tensile Deformation of Dual-Phase Steel, *J. Mater. Eng. Perform.*, 2012, **21**, p 382–387
34. C.R. Brooks, *Principles of the Heat Treatment of Plain Carbon and Low Alloy Steels*, ASM International, OH, 1996
35. Q. Jia, W. Guo, P. Peng, M. Li, Y. Zhu, and G. Zou, Microstructure- and Strain Rate-Dependent Tensile Behavior of fiber Laser-Welded DP980 Steel Joint, *J. Mater. Eng. Perform.*, 2016, **25**, p 668–676
36. J.H. Hollomon, Tensile Deformation, *Am. Inst. Min. Metall. Eng. Trans. Iron Steel Div.*, 1945, **162**, p 268–289

37. P. Ludwik, *Elements of Technical Mechanics*, Springer, Berlin, 1909
38. P. Movahed, S. Kolahgar, S.P.H. Marashi, M. Pournvari, and N. Parvin, The Effect of Intercritical Heat Treatment Temperature on the Tensile Properties and Work Hardening Behavior of Ferrite-Martensite Dual Phase Steel Sheets, *Mater. Sci. Eng. A*, 2009, **518**, p 1–6
39. Y. Mazaheri, A. Kermanpur, A. Najafizadeh, and N. Saeidi, Effects of Initial Microstructure and Thermomechanical Processing parameters on Microstructures and Mechanical Properties of Ultrafine Grained Dual Phase Steels, *Mater. Sci. Eng. A*, 2014, **612**, p 54–62
40. J. Kadkhodapour, A. Butz, and S.Z. Rad, Mechanisms of Void Formation During Tensile Testing in a Commercial, Dual-Phase Steel, *Acta Mater.*, 2011, **59**, p 2575–2588